sciendo

POLISH MARITIME RESEARCH 1 (121) 2024 Vol. 31; pp. 24-34
10.2478/pomr-2024-0003

HYDRODYNAMIC LOADS ON A SEMI-SUBMERSIBLE PLATFORM SUPPORTING A WIND TURBINE UNDER A MOORING SYSTEM WITH BUOYS

Thomas Mazarakos [1]
Theodosis Tsaousis [2]
[1] Department of Naval Architecture, School of Engineering, University of West Attica, Egaleo, Attica, Greece
[1] School of Naval Architecture and Marine Engineering, National Technical University of Athens, Zografos Campus, Athens, Greece

* Corresponding author: *tmazar@uniwa.gr (T. Mazarakos)*

ABSTRACT

In this study, the effect of a 10MW DTU wind turbine (WT) on a semi-submersible platform is examined from the point of view of its dynamic behaviour as part of a mooring system with attached buoys. The platform has a rectangular geometry, and consists of four offset and one main cylindrical members. The structure is assumed to receive both wave and wind loading simultaneously. A coupled analysis within the frequency domain is performed using two boundary element method software packages, NEMOH and HAMS. The results are presented in the form of parametric graphs for each of the software packages used and for varying wave directions. The graphs show the hydrodynamic loads exerted on the platform, the wave elevation, the added masses, the hydrodynamic damping coefficients, the mooring line tensions, and the Response Amplitude Operators (RAOs) for the motion of the platform.

Keywords: Hydrodynamic loads; Semi-submersible platform; Wind turbine; Mooring system; Catenary line; Buoys; RAO

INTRODUCTION

Solar, wind and wave energy are unquestionably some of the cleanest forms of energy. Both on land and at sea, they can offer essential resources for the production of electrical power that is sufficient to cover the needs of thousands of homes. It is also clear that the development of alternative forms of energy contributes to the reduction of greenhouse emissions.

In particular, the design of offshore structures for the exploitation of these natural resources, and consequently for the production of renewable energy, is a continuously growing field of research, since most of these technologies are still in their infancy. Despite their limited efficiency compared to onshore renewable systems, several types of structures have been designed with the intention of utilising the vast available potential lying offshore. Floating photovoltaics (FPV) systems have been developed relatively recently in Portugal, Brazil, Japan, and other countries worldwide, and research on installation locations, cooling mechanisms, efficiency improvements and mooring systems is available in the literature [1-5].

The general principle of operation of a wave energy converter (WEC) is based on the action of waves to produce electricity. There are many types and configurations that have been discussed in the literature [6-9]. Studies of mooring systems for WECs can be found in references [10-13]. More sophisticated hybrid designs have been developed that combine oscillating water column (OWC) devices with floating wind turbines (WTs) [14, 15].

Offshore WTs are used to exploit the potential offered by the wind out at sea. Depending on the water depth in the region of installation, they are either fixed to the bottom of the sea or are allowed to float. The most common types of fixed systems are monopiles and jacket structures [16-19]. However, when the water depth is greater than 50 m, floating structures are needed. Floating WTs may be cost-effective at depths where fixed WTs

are impossible to install, or where the cost is excessively high due to large water depths. One type of structure is a spar-buoy, typically in the form of a cylindrical floater that supports the WT [20-22]. Another type is a semi-submersible platform, which consists of one main, central and some offset cylinders, the exact number of which depends on the geometry of the floater [23, 24]. Fully coupled hydro-aero-elastic analyses of this structure were conducted in [25, 26].

A floating structure is moved from its initial equilibrium position by the forces exerted on it through the combined action of waves and wind. A design that includes a suitable mooring system is therefore urgently needed. A typical fixed structure used in deep water is a Tension Leg Platform (TLP) [27-30]. In this case, the floating structure is permanently moored using tendons, which restrict the platform to very small heave motions due to the large pretension along the z-axis.

Taut-leg mooring lines are also used; in this case, the mooring cables form an angle with the seabed, and the anchoring point needs to withstand both horizontal and vertical forces. Another type of mooring system is based on the use of catenary lines which lie horizontally at the seabed, and may also include clump weights or buoys [31, 32]. A finite difference analysis of a catenary riser was presented in [33]. The buoys may either be positioned at the surface or fully submerged to provide some additional buoyancy, in which case the weight on the mooring lines is decreased and their dynamic behaviour and performance are enhanced. The impact of using submerged buoys on the dynamic tension of the mooring line was numerically and experimentally investigated in [34]. The use of buoys can decrease the tension, provided that their position, size, and number are carefully considered. In order to assess the impact of submerged buoys on the dynamic behaviour of the mooring line, the previous study was extended by using numerical methods in the time and frequency domains [35]. The effects of two hybrid taut mooring lines on the motion of a semi-submersible platform and the tension in these lines have also been studied [36]. These systems combine the use of weights and buoys along the mooring line. In [37], the authors discussed the effects of buoys on the dynamics of a semi-submersible platform, and explored how the system's operational capacity could be increased by adding more buoys to the system in deep and very deep waters. Finally, several configurations of catenary and taut mooring systems for a semi-submersible 5MW WT in shallow waters, involving different materials, mooring components and anchors, were examined in [38]. The material of the mooring lines has also been found to be a key parameter affecting the strength of the system [39, 40].

In this study, we perform a coupled analysis of a catenary line with buoys. The solution to this problem is split into two main parts: firstly, we need to identify how the WT affects the dynamics of the coupled problem, and secondly, we need to solve for the motion of the total floating structure. The effect of the WT is defined by means of inertial, gyroscopic, and gravitational effects, as well as aerodynamic loading. We therefore need to calculate the added mass, damping and stiffness matrices of the WT. To this end, a Hamiltonian dynamic analysis based on blade element momentum theory is employed. This issue is not elaborated in detail within this particular study, and the reader is referred to the literature instead. The hydrodynamic part of the problem was solved using the open-source codes NEMOH [41] and HAMS [42].

GEOMETRY OF THE SEMI-SUBMERSIBLE PLATFORM AND THE CLUMP BUOYS MOORING SYSTEM

The semi-submersible platform considered here accommodates a 10 MW DTU WT [43]. The water depth at the installation site is 200 m, and the draft of the floating platform is 20 m. A three-dimensional schematic representation of the platform and the mooring system is provided in Figure 1. The floater is rectangular, and is composed of one main, central column and four offset column-cylindrical tubes at each corner of the floater. Thinner, horizontal, and inclined tubular members connect these members to provide the required buoyancy, along with cross braces. Top and side views of the floater are shown in Figures 2 and 3. To reach the top of the main column of the floating platform, the tower of the WT is cantilevered at a height of 10 m above the still water level (SWL). For the purposes of this study, the main parts of the WT that are considered in the analysis are the rotor-nacelle assembly, the tower, and the three blades.

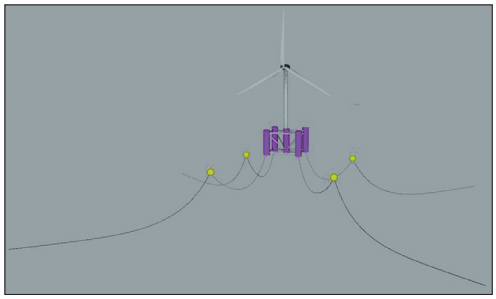

Fig. 1. Rectangular semi-submersible platform supporting the 10MW WT, shown in 3D with the mooring system and buoys

In the static equilibrium position in still water, the platform has a mass of 7,728,000 kg, including all the weights involved and any additional ballast that may be required. The platform's centre of mass (CM), including the ballast, is located along its centreline and 9.91 m below the SWL. The roll and pitch inertias are 7,730,000,000 kgm^2, while the yaw inertia is 6,700,000,000 kgm^2.

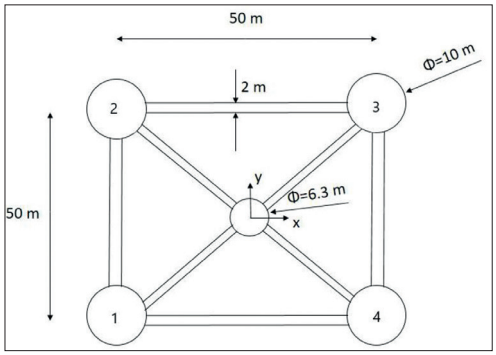

Fig. 2. Top view of the rectangular semi-submersible platform

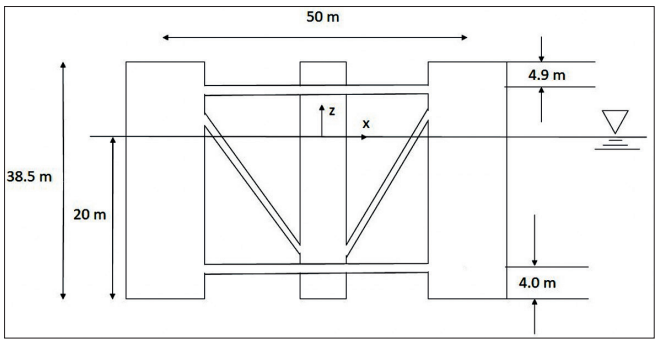

Fig. 3. Right side view of the rectangular semi-submersible platform

Four catenary lines make up the mooring system, each of which has a buoy attached to it. All of mooring lines (and their segments) are made from the same material (R4-RQ4, studless chain, steel). The selected geometrical configuration for the mooring system ensures a zero total sum of the forces in the horizontal and transversal directions. Table 1 lists the mechanical, geometrical and physical characteristics of the mooring system. The points at which the mooring lines are attached to the platform are 14 m below the free surface, and their respective coordinates are given in Table 2.

Tab. 1. Physical, geometrical and mechanical properties of the mooring system with buoys

Number of mooring lines (two elements each, separated by an attached buoy)	4
Angle between two consecutive lines	90°
Water depth	200 *m*
Depth to fairleads below SWL	14 *m*
Radius of the mooring system measured from the cenre of the platform	635 *m*
Radius of the mooring lines attachment points measured from the centre of the platform	40.868 *m*
Total length of the mooring lines	835.5 *m*
Length of the first segment	484.5 *m*
Length of the second segment	351.0 *m*
Diameter of first segment	0.087 *m*
Diameter of first segment	0.040 *m*
Mass of the lines per unit length in the air (first segment)	151*kg/m*
Mass of the lines per unit length in the air (second segment)	30.00*kg/m*
Weight of the lines per unit length in the water (first segment)	1400 *N/m*
Weight of the lines per unit length in the water (second segment)	240 *N/m*
Buoy's Net Buoyancy (*NB*)	176000 *N*
Pretension at the top of each mooring line (*Tp*)	600000 *N*
Stiffness of mooring lines *Kxx* = *Kyy*	140000 *N/m*

Tab. 2. Coordinates of the mooring lines

Mooring line (#)	Upper attachment point (*x*, *y*, *z*)	Lower attachment point (*x*, *y*, *z*)
1	(–28.56, –28.56, –14)	(–449, –449, –200)
2	(–28.56, 28.56, –14)	(–449, 449, –200)
3	(28.56, 28.56, –14)	(449, 449, –200)
4	(28.56, –28.56, –14)	(449, –449, –200)

By identifying the forces acting on an element of the mooring line (in the 2D xz-plane), we can obtain the following two generic equations for the normal and tangential directions [44; p.258]

$$dT - \rho g A dz = [w\sin\varphi - F(1+\frac{T}{EA})]ds \quad (1)$$

$$Td\varphi - \rho g A z d\varphi = [w\cos\varphi + D(1+\frac{T}{EA})]ds \quad (2)$$

where D and F are the mean hydrodynamic forces per unit length in the normal and tangential directions, respectively, w is the weight per unit length of the line in the water, A is the cross-sectional area of the mooring line, E is the elastic modulus, T is the line tension, φ is the angle between the line and the horizontal, and s is an independent parameter along the mooring line. Figure 4 shows a 3D view of the suspended mooring line system, while Figure 5 shows the configuration of one mooring catenary line under various external forces.

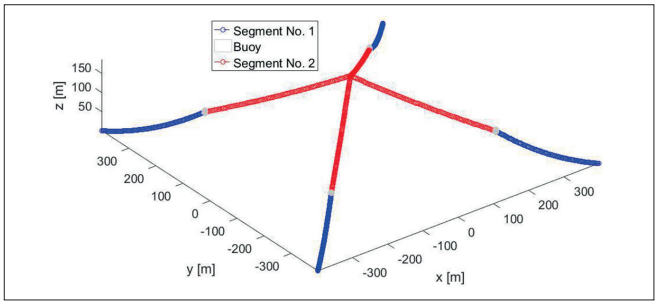

Fig. 4. 3D view of the suspended mooring line system

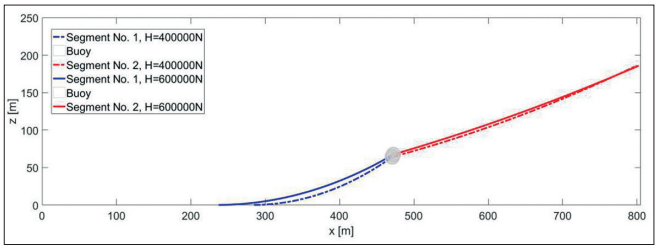

Fig. 5. One-line configuration under different external forces

DISCRETIZATION OF THE FLOATING STRUCTURE AND A FULLY COUPLED ANALYSIS

SOLUTION TO THE HYDRODYNAMIC PROBLEM

As discussed in the introduction, the solution to the coupled problem is found by solving the hydroelastic problem and quantifying the contribution of the WT, by calculating the

added mass, damping and stiffness matrices of the WT (which are superimposed onto those of the floating structure).

The hydrodynamic problem is addressed in the context of the boundary element method (BEM). We treat the problem in 3D, assuming an incompressible, inviscid and irrotational flow so that the linear potential theory can be utilised, and the coordinate system is defined in Figures 2 and 3. For the hydrodynamic calculations of this study, we use BEM solvers called NEMOH and HAMS. NEMOH is an open-source BEM solver developed by the Ecole Centrale de Nantes [41], which solves the linear boundary value problem by using a generalised mode approach and source distribution for the Green function. In the literature, comparisons of results obtained using NEMOH with those from the well-known BEM solver WAMIT have demonstrated satisfactory accuracy. In addition to NEMOH, we also used the open-source BEM solver HAMS, again using the potential flow theory, with a code written in the FORTRAN 90 language [42]. The solver uses boundary integral equations to represent the scattered wave potentials. In both cases, the solvers give several outputs, but the ones considered in this study are the first-order hydrodynamic coefficients, i.e., the added mass, the radiation damping and excitation forces. We also note that the motions of the floater are calculated only with HAMS, as NEMOH v.2 does not allow for calculation of the RAOs of the structure.

In order to solve the problem numerically, the wetted surface of the structure is subdivided into plane facets with a triangular or quadrilateral shape. The panel subdivision of the configuration used here is depicted in Figures 6 and 7. A total of 1500 elements were used to discretise the wetted surface of the body in NEMOH (without the braces), and 7,696 elements were used for discretisation with HAMS (with the braces).

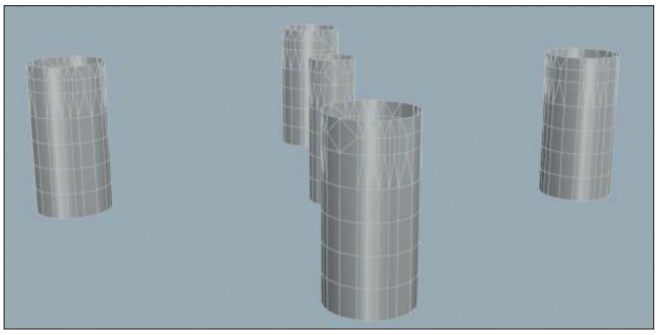

Fig. 6. Panel discretization – NEMOH

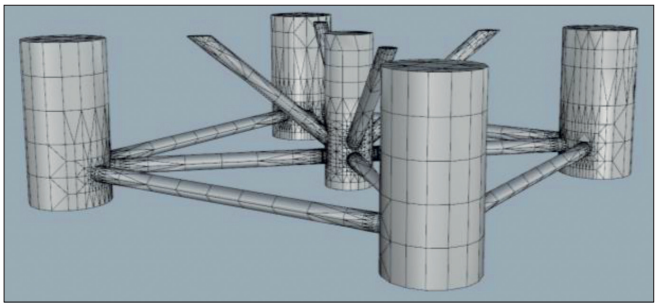

Fig. 7. Panel discretization – HAMS

The impact of the WT on the dynamic behaviour of the floater also needs to be discussed. Due to the presence and operation of the WT (including gravitational and inertial/gyroscopic effects, and aerodynamic loading), the forces owing to the added masses, damping coefficients, and stiffness coefficients actually superinduce the external loads. Nevertheless, given that the purpose of our study is to focus on the dynamic behaviour of a floating structure subjected to external wind and wave loads, an aerodynamic analysis of the WT is not carried out. The reader is referred to [29] for more details on this issue.

The total mass of the WT is 1,200,000 kg and mass of the tower is 563,000 kg. The mass of the hub is 106,000 kg, and that of the nacelle is 406,000 kg (Figure 1).The total mass of the three blades is 126,000 kg [43].

COUPLED EQUATIONS OF MOTION

After obtaining the solution to the hydrodynamic boundary value problem and defining the multifaceted effects of the WT, we now calculate the responses of the platform. Following Newton's second law, the coupled dynamic equations of motions can be described as follows [29]:

$$\Sigma_{j=1}^{6}\left\{-\omega^2\left[(M_{ij}+A_{ij})+A_{ij}^{WT}+\frac{i}{\omega}(B_{ij}+B_{ij}^{WT})\right]+ C_{ij,\,hydro}+C_{ij,\,mooring}+C_{ij}^{WT}\right\}x_{j0}=F_i,\ \ i=1,\ldots,6 \quad (3)$$

where

M_{ij} : mass of the platform
A_{ij} : added mass
B_{ij} : hydrodynamic damping
$C_{ij,\,hydro}$: hydrostatic stiffness
$C_{ij,\,mooring}$: stiffness coefficients of the mooring lines
F_i : first-order wave loads, matrices of the floating platform

The equations of motion are solved in the frequency domain. The matrices of the WT are denoted as follows:
A_{ij}^{WT} : added mass
B_{ij}^{WT}: damping
C_{ij}^{WT}: stiffness.

In this approach, the contribution of the WT is modelled as an external loading due to inertial, gyroscopic, gravitational, and aerodynamic effects, by introducing the last three of these matrices (subscript WT) into the dynamic equation of motion of the floating platform.

The hydrodynamic pressures are integrated over the entire wetted surface of the floater to derive the exciting forces on the right-hand side of Equation (3). These hydrodynamic pressures are caused by (i) the potential arising from the incident wave, and (ii) the diffraction/radiation potential. They are calculated in a straightforward way with the aid of Bernoulli's equation.

NUMERICAL RESULTS: COMPARISON AND DISCUSSION

In this section, we present the most important numerical results. We compare the exciting forces to those originating from the added masses and damping coefficients for the floating structure, both with and without braces. The figures cited here represent the RAOs of the motions of the floating platform. Particular attention is also paid to the free surface elevation around the floating structure,

both in 2D and 3D, as well as to the mooring tensions exerted on the mooring lines at the point where they are attached to the floater (for the coordinates of this point, see Table 2). Finally, the results are discussed in terms of the wave direction, the wave frequency, and the qualitative behaviour of each graph, and their maximum values. The numerical results presented in the following correspond to regular waves of height H = 2 m.

EXCITING FORCES AND MOMENTS

The excitation forces and the wave moments are calculated with the aid of NEMOH and HAMS software. More details can be found in [41, 42]. The wave forces are derived by integrating the hydrodynamic pressures acting on the wetted part of the floater. The potential of the incident wave and the diffraction potential are considered in the calculation of the hydrodynamic pressures. By exploiting the linearised Bernoulli equation, the following general form of Equation (4) is derived:

$$F_i = -i\omega\rho \iint_s \varphi n dS \tag{4}$$

where φ is the incident and diffracted potential, n is the normal vector pointing outwards from the wetted surface into the fluid, and S denotes the wetted surface. Similarly, the overturning moments acting on the floating structure are given by Equation (5):

$$M_i = -i\omega\rho \iint_s \varphi(x \times n) dS \tag{5}$$

Figures 8–10 show the first-order wave loads and moments for a range of angular frequencies and wave directions. Due to the double symmetry of the rectangular floater, the forces Fy and the moments Mx are omitted.

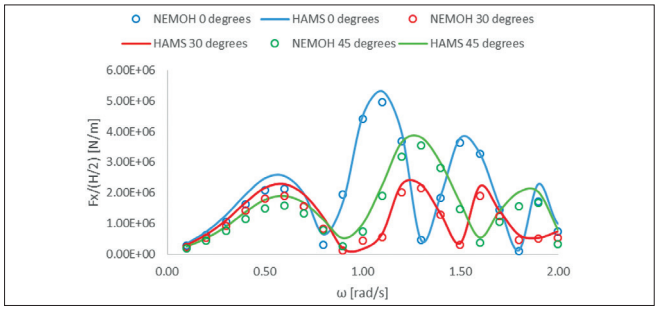

Fig. 8. First-order wave loads in the direction exerted on the floating platform versus ω for wave headings of 0°, 30° and 45°

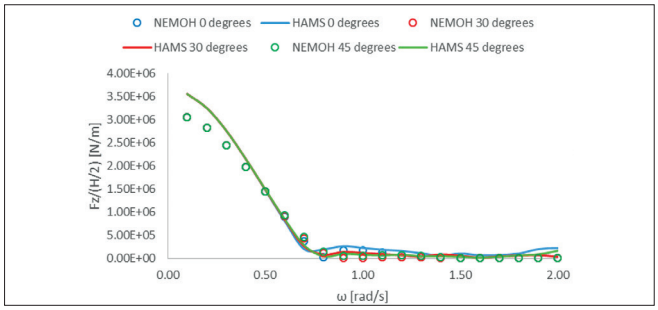

Fig. 9. First-order wave loads in the direction exerted on the floating platform versus ω for wave headings of 0°, 30° and 45°

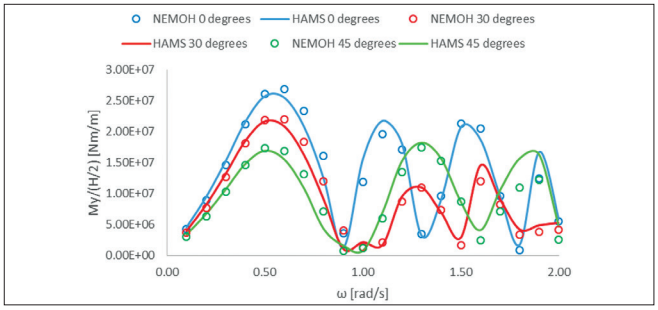

Fig. 10. First-order wave loads My on the floating platform versus ω for wave headings of 0°, 30° and 45°

From Figures 8–10, it can be observed that all the curves obtained from NEMOH and HAMS follow the same trend. The horizontal forces presented in Figure 8 form three peaks, with the first one at ω = 0.6 rad/s, while the second (with a higher value) and third clearly depend on the wave heading. The vertical forces start with a maximum value at ω = 0.1 rad/s, and then decrease drastically at ω = 0.8 rad/s. The curves related to the bending moments around the y-axis follow a similar trend to those of the horizontal forces, but for wave headings of 0° and 30°, the maximum value is seen for the first peak, and specifically at ω = 0.6 rad/s. All of these behaviours are attributed to the interactions between the cylinders and the incoming regular waves.

WAVE ELEVATION ARROUND THE PLATFORM

In this section, the free surface elevation around the structure is discussed for values of ω = 0.6 rad/s with a wave heading 0°, ω = 1.1 rad/s for a wave heading of 30°, and ω = 1.6 rad/s for a wave heading of 45°, using the open-source code NEMOH. These frequencies are considered due to the fact that the exciting forces reach a peak at these values, as described in the previous section.

In potential flow theory, the free surface elevation is given in terms of the velocity potential (which is actually derived based on the kinematic condition of the free surface at $z = 0$), as shown in Equation (6):

$$\eta = \frac{i\omega}{g}\frac{\partial\varphi}{\partial t} \tag{6}$$

where η denotes the free surface elevation, and φ represents the incident wave and diffraction potentials.

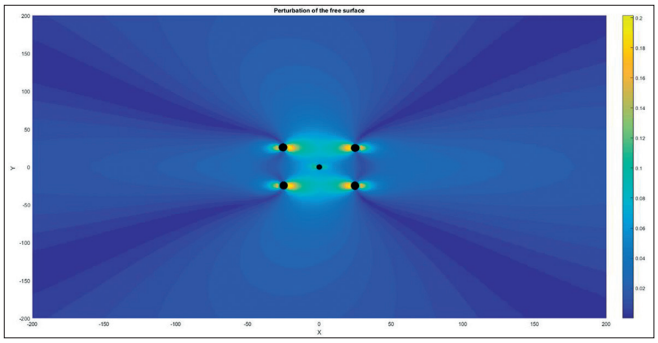

Fig. 11. 2D perturbation of the free surface around the floating structure for ω = 0.6 rad/s and wave heading 0°

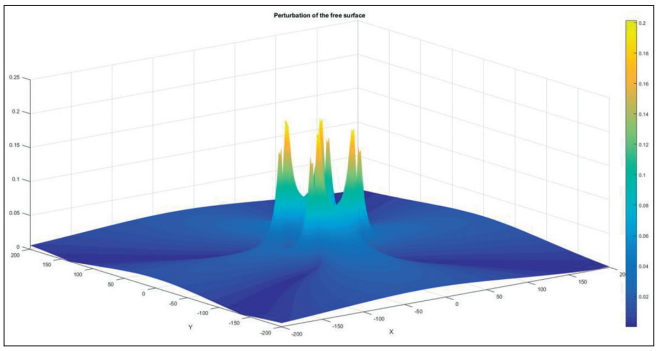

Fig. 12. 3D perturbation of the free surface around the floating structure for ω = 0.6 rad/s and wave heading 0°

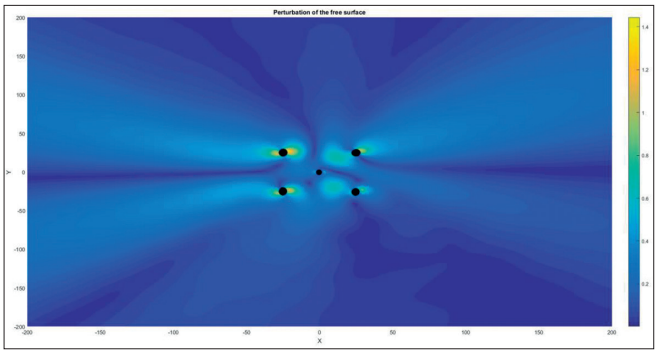

Fig. 13. 2D perturbation of the free surface around the floating structure for ω = 1.1 rad/s and wave heading 3°

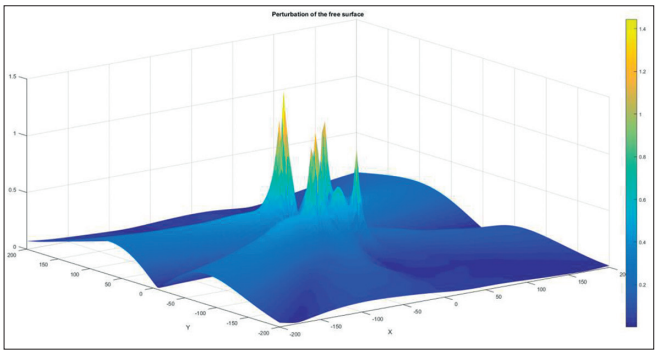

Fig. 14. 3D perturbation of the free surface around the floating structure for ω = 1.1 rad/s and wave heading 30°

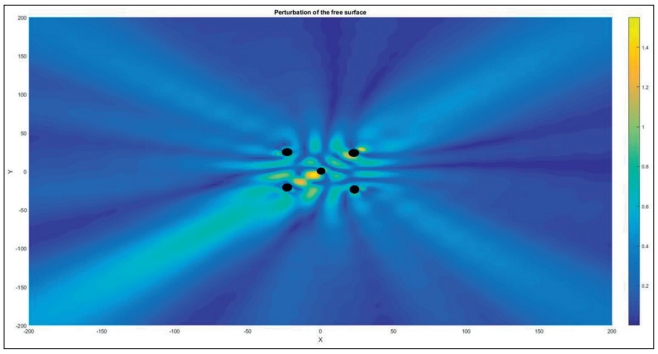

Fig. 15. 2D perturbation of the free surface around the floating structure for ω = 1.6 rad/s and wave heading 45°

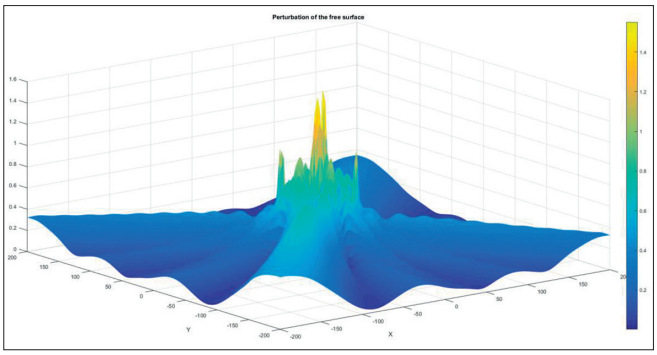

Fig. 16. 3D perturbation of the free surface around the floating structure for ω = 1.6 rad/s and wave heading 45°

At ω = 0.6 rad/s (Figures 11, 12), the maximum value of the free surface elevation is approximately 0.2, around the four offset cylindrical tubes. At ω = 1.1 rad/s (Figures 13, 14), the free surface elevation obtains its maximum value of approximately 1.4, at the back of the second offset cylinder of the floating structure (see Figure 2). Finally, at ω = 1.6 rad/s (Figures 15, 16), the maximum value is around 1.5 at a position between the first cylinder and the main central column of the floater.

ADDED MASSES AND HYDRODYNAMIC DAMPING OF THE FLOATER

The behaviour of the added mass coefficients as a function of the incident wave frequency is shown in Figures 17 and 18, while the behaviour of various damping coefficients is shown in Figures 19 and 20. As discussed above, these hydrodynamic parameters were explicitly derived from the two software packages that were used in this study [41, 42].

The solution to the radiation problem is related to the added mass and damping matrices; as depicted in the following graphs, these coefficients are frequency-dependent.

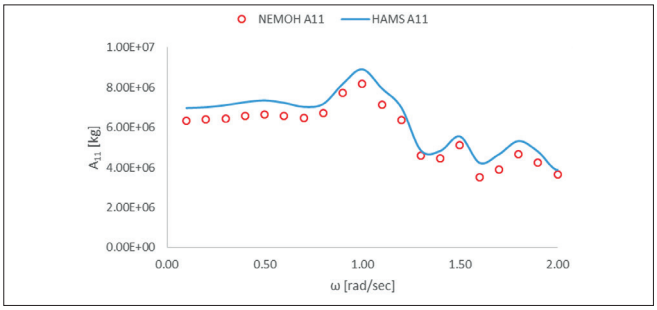

Fig. 17. A_{11} as a function of the wave frequency

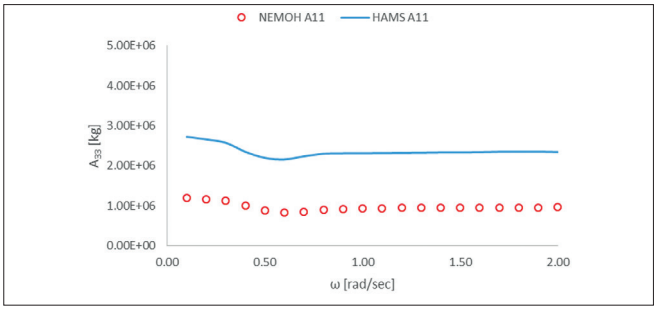

Fig. 18. A_{33} as a function of the wave frequency

From Figure 18, a pronounced difference between the two graphs can be observed. This can be attributed to whether or not the brackets that interconnect the cylindrical columns of the floating structure are included in the discretisation needed for the solution to the hydrodynamic problem. More specifically, although the curves follow the same qualitative trend, when HAMS is used (i.e., the brackets are taken into account), the A_{33} added masses are approximately 1500 t larger than those predicted by NEMOH, where the brackets are excluded from the discretisation. This difference is equal to the additional buoyancy due to the brackets of the floater. This is because when the brackets are included in the discretisation of the structure, the displacement volume of the structure is greater, and hence the additional mass is greater. Consequently, in order to ensure a more precise calculation of the movements of the floating structure, the brackets should be included in the discretisation.

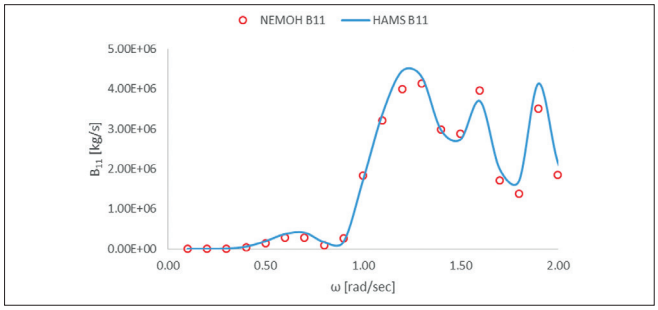

Fig. 19. B_{11} as a function of wave frequency

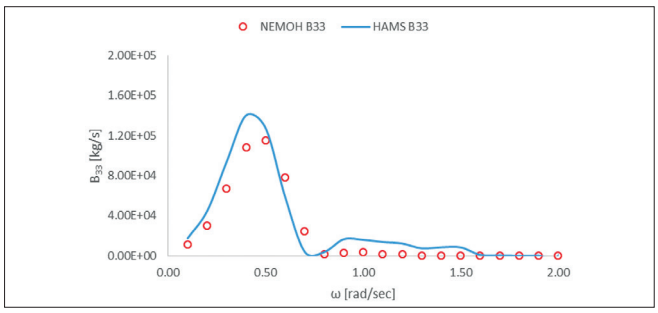

Fig. 20. B_{33} as a function of wave frequency

MOTION OF THE FLOATING PLATFORM

In this subsection, we present some numerical results for the RAOs of the platform. It was assumed for these calculations that the wind speed was 11.4 m/s. Figures 21 and 22 show the RAOs of the surge and heave motions of the floater. These RAOs are nondimensionalised by the term H/2, which is the wave amplitude, where H is the wave height (H = 2 m). Due to the double symmetry of the platform, the sway motions are not considered here; as expected, they exhibit an analogous configuration with the surge motions, relative to the direction of the incoming wave. As expected from a physical analysis, when the incoming wave is parallel to the x-axis, the surge motion is higher (β = 0°), and this decreases as the wave's direction becomes vertical to the x-axis (or equivalently parallel to the y-axis) (see Figure 2). We also observe that all the curves start from an initial maximum value at ω = 0.1 rad/s which then decreases rapidly, with an explicit (although significantly smaller) peak at ω = 0.3 rad/s. For greater values of the wave frequency, the platform is only very slightly affected.

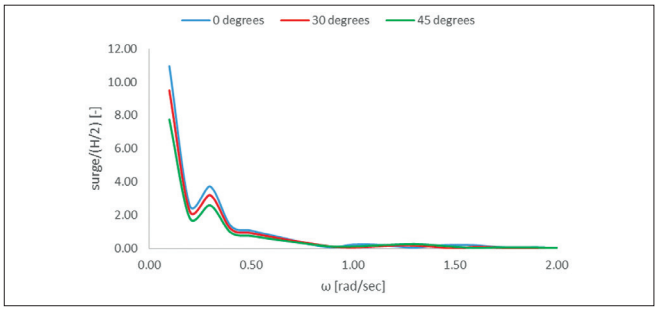

Fig.21. Surge RAOs for the floating platform with the WT, for three different directions of the incident wave, under the buoy mooring system

Figure 22 shows the RAOs of the heave motion of the floater. The heave motions have a particular feature: the curves for ω = 0.1 to 0.7 rad/s and ω = 1.1 to 2.0 rad/s coincide, for each pair of directions. The heave motion reaches a maximum value of 1.453 at ω = 0.8 rad/s and the corresponding curve then exhibits an abrupt decrease. We can also observe that the vertical motion of the platform is practically zero for all wave directions when ω > 1.7 rad/s.

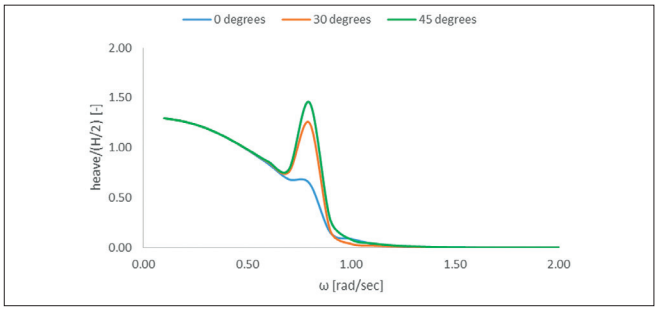

Fig. 22. Heave RAOs for the floating platform with the WT for three different directions of the incident wave, under the buoy mooring system

Figure 23 shows the results for the pitch motion of the platform. Once again, the graph for the roll motion is neglected here, since it is analogous to the pitch motion, as expected. The RAOs of the rotational motions are nondimensionalised by the term kH/2, where k is the wavenumber. The maximum rotation around the y-axis is obtained when the x-axis is parallel to the incident wave. Its value is 5.678 for a wave frequency of ω = 0.3 rad/s.

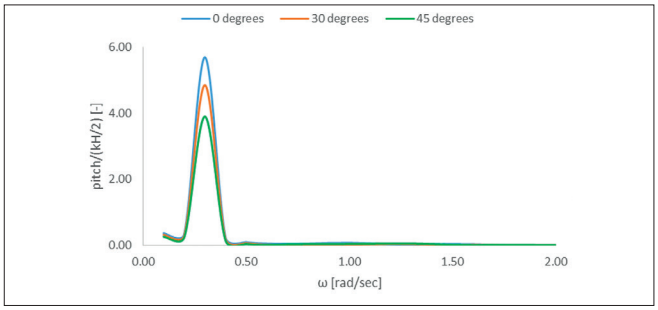

Fig. 23. Pitch RAOs for the floating platform with the WT for seven different directions of the incident wave, under the buoy mooring system

MOORING LINE TENSIONS

Neither NEMOH and HAMS could be used to calculate the tensions exerted on the floating structure by the mooring system. However, by applying the method presented in [30, 45] the tension in each branch of the mooring system was obtained. Figs. 24–27 present the tensions of the mooring system for three different wave headings of 0°, 30° and 45°.

The first observation that can be made is that all the curves follow a similar trend. We can also see that the mooring tensions are only slightly affected by the wave heading, and that the relevant discrepancies are small. The maximum mooring forces are seen at ω = 0.1 rad/s, and decrease drastically with increasing ω. In addition, as can be seen in Figures 24 and 25, there is an initial peak at ω = 0.3 rad/s and a smaller secondary one at ω = 0.8 rad/s. Moreover, the mooring tensions become greater at a wave heading of 45° in all cases. Finally, for ω > 1.5 rad/s, the mooring tensions tend practically to zero.

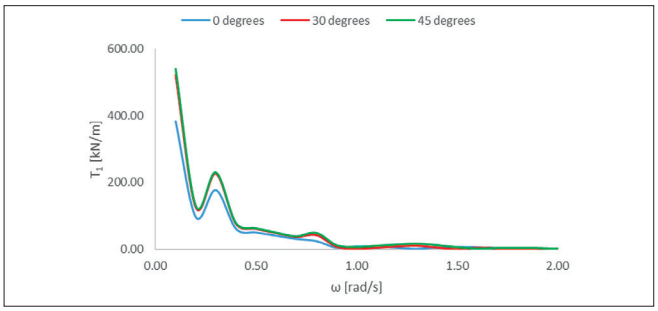

Fig. 24. Total mooring forces on the first mooring line

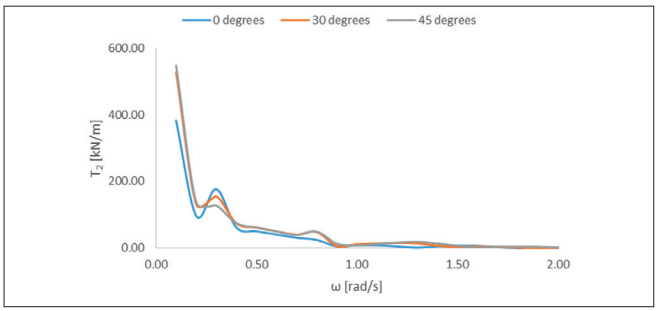

Fig. 25. Total mooring forces on the second mooring line

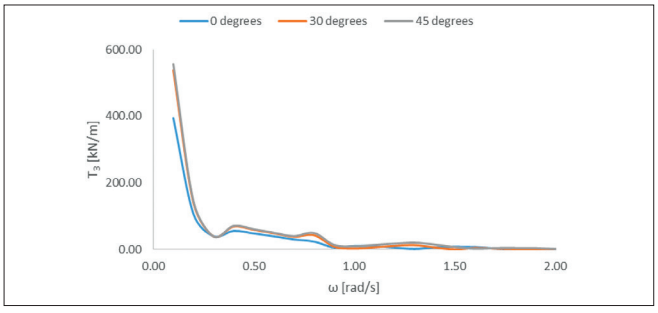

Fig. 26. Total mooring forces on the third mooring line

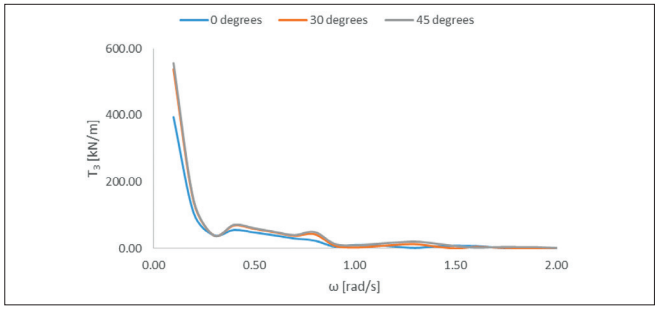

Fig. 27. Total mooring forces on the fourth mooring line

CONCLUSION

The aim of this study was to analyse the dynamic behaviour of a semi-submersible platform supporting a 10MW WT, under a four-branch mooring system with buoys. To this end, a coupled analysis was employed. It was assumed that the wind speed was 11.4 m/s. The hydrodynamic boundary value problem was solved numerically using two BEM software packages called NEMOH and HAMS. The added masses, damping coefficients, and stiffness matrices of the WT were taken into consideration in order to reduce and incorporate the gravitational, inertial, gyroscopic, and aerodynamic effects of the WT on the floating structure. The results were examined primarily in terms of the impact of the wave heading and angular frequency on the maximum values of the physical quantities under consideration. The hydrodynamic behaviour of the floater was examined both with and without braces.

Several numerical results were presented for the RAOs of the floater, and the exciting forces were compared to those originating from the added masses and damping coefficients of the floating structure, with and without braces. The curves of the exciting forces were found to follow a similar pattern, while the wave heading seemed to have an influence on the incoming wave frequency at which the maximum value appeared. For the RAO of the surge motion, it was found that all the curves started from an initial maximum value at ω = 0.1 rad/s and then decreased rapidly, with a pronounced but much smaller peak at ω = 0.3 rad/s. In regard to the heave motion, the curves coincided for specific directions of the incoming wave, and the same effect was also observed for the yaw motion. The maximum value for the RAO of the pitch was reached at ω = 0.3 rad/s. The position of the maximum value of free surface elevation was not constant, and clearly depended on the wave frequency. The mooring tensions were not greatly affected by the wave heading. The relevant curves started from a maximum value and then formed two more peaks with a significantly smaller magnitude. Finally, in all cases, the mooring tensions tended to zero for ω > 1 rad/s.

ACKNOWLEDGEMENTS

This research was funded by the "Special Account for Research Grants (ELKE) " of the University of West Attica.

REFERENCES

1. L. Liu, Q. Sun, H. Li, H. Yin, X. Ren, and R. Wennersten, "Evaluating the benefits of integrating floating photovoltaic and pumped storage power system," Energy Conversion and Management, Vol. 194, pp. 173-185, 2019, doi.org/10.1016/j.enconman.2019.04.071.

2. G. Da Silva and D. Branco, "Is floating photovoltaic better than conventional photovoltaic? Assessing environmental impacts," Impact Assessment and Project Appraisal, Vol. 36(5), pp. 390-400, 2018, doi.org/10.1080/14615517.2018.1477498.

3. S. Kim, Y. Lee, S. Seo, H. Joo, and S. Yoon, "Structural design and installation of tracking-type floating PV generation system," Composites Research, Vol. 27(2), pp. 59-65, 2014, doi.org/10.7234/composres.2014.27.2.059.

4. B. Chico Hermanu, B. Santoso, S. Suyitno, and F. Wicaksono, "Design of 1 MWp floating solar photovoltaic (FSPV) power plant in Indonesia," AIP Conference Proceedings, Surakarta, Indonesia, 9-11 October, 2019, doi.org/10.1063/1.5098188.

5. E. Do Sacramento, P. Carvalho, J. De Araujo, D. Riffel, R. Da Cruz Correa, and J. Neto, "Scenarios for use of floating photovoltaic plants in Brazilian reservoirs," IET Renewable Power Generation, Vol. 9(8), pp. 1019-1024, 2015, doi.org/10.1049/iet-rpg.2015.0120.

6. X. Zhao, X. Du, M. Li, and M. Goteman, "Semi-analytical study on the hydrodynamic performance of an interconnected floating breakwater-WEC system in presence of the seawall," Applied Ocean Research, Vol. 109, 2021, doi.org/10.1016/j.apor.2021.102555.

7. B. Guo, Q. Elmoosa, C. Windt, and J. Ringwood, "Impact of nonlinear hydrodynamic modelling on geometric optimization of a spherical heaving point absorber," 14th European Wave and Tidal Energy Conference, Plymouth, UK, 5-9 September, 2021.

8. S. Michele and E. Renzi, "A second-order theory for an array of curved wave energy converters in open sea," Journal of Fluids and Structures, Vol. 88, pp. 315-330, 2019, doi.org/10.1016/j.jfluidstructs.2019.05.007.

9. D. Evans and R. Porter, "Efficient calculation of hydrodynamic properties of OWC type devices," Journal of Offshore Mechanics and Arctic Engineering, Vol. 119(4), pp. 210-218, 1997, doi.org/10.1115/1.2829098.

10. J. Fitzgerald and L. Bergdahl, "Considering mooring cables for offshore wave energy converters," 7th European Wave and Tidal Energy Conference, Porto, Portugal, 11-13 September, 2007.

11. J. Fitzgerald and L. Bergdahl, "Including moorings in the assessment of a generic offshore wave energy converter: A frequency domain approach," Marine Structures, Vol. 21(1), pp. 23-46, 2008, doi.org/10.1016/j.marstruc.2007.09.004.

12. L. Johanning and G. Smith, "Improved measurement technologies for floating wave energy converter (WEC) mooring arrangements," Underwater Technology, Vol. 27(4), pp. 175-184, 2008, doi.org/10.3723/ut.27.175.

13. S. Yang, J. Ringsberg, E. Johnson, Z. Hu, and J. Palm, "A comparison of coupled and de-coupled simulation procedures for the fatigue analysis of wave energy converter mooring lines," Ocean Engineering, Vol. 117(1), pp. 332-345, 2016, doi.org/10.1016/j.oceaneng.2016.03.018.

14. T. Mazarakos, D. Konispoliatis, D. Manolas, S. Mavrakos, and S. Voutsinas, "Coupled hydro-aero-elastic analysis of a floating structure for offshore wind and wave energy sources exploitation," 12th International Conference on Stability of Ships and Ocean Vehicles, Glasgow, Scotland, UK, 14-19 June, 2015.

15. T. Mazarakos, D. Konispoliatis, D. Manolas, S. Voutsinas, and S. Mavrakos, "Modelling of an offshore multi-purpose floating structure supporting a wind turbine including second-order wave loads," 11th European Wave and Tidal Energy Conference, Nantes, France, 6-11 September, 2015.

16. S. Seng, C. Monroy, and S. Malenica, "Dynamic response of monopile wind turbine in large waves," 38th International Conference on Ocean, Offshore and Arctic Engineering, Glasgow, Scotland, UK, 9-14 June, 2019.

17. K. Maes, W. Weijtjens, E. De Ridder, and G. Lombaert, "Inverse estimation of breaking wave loads on monopile wind turbines," Ocean Engineering, Vol. 163(1), pp. 544-554, 2018, doi.org/10.1016/j.oceaneng.2018.05.049.

18. S. Jalbi and S. Bhattacharya, "Concept design of jacket foundations for offshore wind turbines in 10 steps," Soil Dynamics and Earthquake Engineering, Vol. 139, 2020, doi.org/10.1016/j.soildyn.2020.106357.

19. I. Chen, B. Wong, Y. Lin, S. Chau and H. Huang, "Design and analysis of jacket substructures for offshore wind turbines," Energies, Vol. 9(4), 2016, doi.org/10.3390/en9040264.

20. M. Karimirad and T. Moan, "Wave and wind induced motion response of catenary moored spar wind turbine," 3rd International Conference on Computational Methods in Marine Engineering, Trondheim, Norway, 15-17 June, 2009.

21. M. Karimirad and T. Moan, "Wave- and wind-induced dynamic response of a spar-type offshore wind turbine," Journal of Waterway, Port, Coastal, and Ocean Engineering, Vol. 138(1), 2012, doi.org/10.1061/(ASCE)WW.1943-5460.0000087.

22. T. Utsunomiya, T. Sato, H. Matsukuma, and K. Yago, "Experimental validation for motion of a spar-type floating offshore wind turbine using 1/22.5 scale model," 28th International Conference on Ocean, Offshore and Arctic Engineering, Honolulu, Hawaii, May 31-June 5, 2009.

23. F. Huijs, R. De Bruijn, and F. Savenije, "Concept design verification of a semi-submersible floating wind turbine using coupled simulations," Energy Procedia, Vol. 53, pp. 2-12, 2014, doi.org/10.1016/j.egypro.2014.07.210.

24. M. Hall and A. Goupee, "Validation of a lumped-mass mooring line model with DeepCwind semisubmersible model test data," Ocean Engineering, Vol. 104(1), pp. 590-603, 2015, doi.org/10.1016/j.oceaneng.2015.05.035.

25. T. Mazarakos, D. Manolas, and S. Mavrakos, "Design and hydro-aero-elastic modeling of a multi leg mooring concept for floating wind turbine applications," 16th International Conference on Ecological Vehicles and Renewable Energies, Monte-Carlo, Monaco, 5-7 May, 2021.

26. T. Mazarakos, D. Manolas, and S. Mavrakos, "Design and hydro-aero-elastic modeling of a TLP concept for floating wind turbine applications," 31st International Ocean and Polar Engineering Conference, Rhodes, Greece, 16-21 June, 2021.

27. G. Katsaounis, S. Polyzos, and S. Mavrakos, "An experimental study of the hydrodynamic behavior of a TLP platform for a 5MW wind turbine with OWC devices," 7th International Conference on Computational Methods in Marine Engineering, Nantes, France, 15-17 May, 2017.

28. Y. Bae, M. Kim, and Y. Shin, "Rotor-floater-mooring coupled dynamic analysis of mini TLP-type offshore floating wind turbines," 29th International Conference on Ocean, Offshore and Arctic Engineering, Shanghai, China, 6-11 June, 2010.

29. T. Mazarakos, D. Manolas, T. Grapsas, S. Mavrakos, V. Riziotis, and S. Voutsinas, "Conceptual design and advanced hydro-aero-elastic modelling of a TLP concept for floating wind turbine applications," 1st International Conference on Renewable Energies Offshore, Lisbon, Portugal, 24-26 November, 2014.

30. T. Mazarakos, T. Tsaousis, S. Mavrakos, and I. Chatjigeorgiou, "Analytical investigation of tension loads acting on a TLP floating wind turbine," Journal of Marine Science and Engineering, Vol. 10(3), 2022, doi.org/10.3390/jmse10030318.

31. Z. Yuan, A. Incecik, and C. Ji, "Numerical study on a hybrid mooring system with clump weights and buoys," Ocean Engineering, Vol. 88(15), pp. 1-11, 2014, doi.org/10.1016/j.oceaneng.2014.06.002.

32. N. Bruschi, G. Ferri, E. Marino, and C. Borri, "Influence of clumps-weighted moorings on a spar buoy offshore wind turbine," Energies, Vol. 13(23), 2020, doi.org/10.3390/en13236407.

33. I. Chatjigeorgiou, "A finite differences formulation for the linear and nonlinear dynamics of 2D catenary risers," Ocean Engineering, Vol. 35(7), pp. 616-636, 2008, doi.org/10.1016/j.oceaneng.2008.01.006.

34. S. Mavrakos, V. Papazoglou, M. Triantafyllou, and J. Hatjigeorgiou, "Deep water mooring dynamics," Marine Structures, Vol. 9(2), pp. 181-209, 1996, doi.org/10.1016/0951-8339(94)00019-O.

35. S. Mavrakos and J. Chatjigeorgiou, "Dynamic behaviour of deep water mooring lines with submerged buoys," Computers & Structures, Vol. 64(1-4), pp. 819-835, 1997, doi.org/10.1016/S0045-7949(96)00169-1.

36. C. Ji and Z. Yuan, "Experimental study of a hybrid mooring system," Journal of Marine Science and Technology, Vol. 20, pp. 213-215, 2015, doi.org/10.1007/s00773-014-0260-7.

37. D. Qiao, J. Yan, and J. Ou, "Effects of mooring line with buoys system on the global response of a semi-submersible platform," Brodogradnja, Vol. 65(41), pp. 79-96, 2014.

38. K. Xu, K. Larsen, Y. Shao, M. Zhang, Z. Gao, and T. Moan, "Design and comparative analysis of alternative mooring systems for floating wind turbines in shallow water with emphasis on ultimate limit state design," Ocean Engineering, Vol. 219(1), 2021, doi.org/10.1016/j.oceaneng.2020.108377.

39. J.-T. Wu, J.-H. Chen, C.-Y. Hsin, and F.-C. Chiu, "Dynamics of the FKT system with different mooring lines," Polish Maritime Research, Vol. 26(1), pp. 20-29, 2019, doi.org/10.2478/pomr-2019-0003.

40. H. Zhang, J. Zeng, B. Jin, C. Chou, H. Li, and H. Dong, "Experimental study of the nonlinear behaviour of deep-sea mooring polyester fibre ropes," Polish Maritime Research, Vol. 30(3), pp. 153-162, 2023, doi.org/10.2478/pomr-2023-0048.

41. A. Babarit and G. Delhommeau, "Theoretical and numerical aspects of the open source BEM solver NEMOH," 11th European Wave and Tidal Energy Conference, Nantes, France, 6-11 September, 2015.

42. L. Yingyi, "HAMS: A frequency-domain preprocessor for wave-structure interactions—Theory, development, and application," Journal of Marine Science and Engineering, Vol. 7(3), 2019, doi.org/10.3390/jmse7030081.

43. C. Bak, F. Zahle, R. Bitsche, T. Kim, A. Yde, L. Henriksen, A. Natarajan, and M. Hansen, "Description of the DTU 10 MW reference wind turbine," Wind Energy Report-I-0092, 2013.

44. O. Faltinsen, Sea loads on ships and offshore structures. Cambridge University Press, Ocean Technology Series, 1990.

45. T. Mazarakos, D. Konispoliatis, G. Katsaounis, S. Polyzos, D. Manolas, S. Voutsinas, T. Soukissian, and S. Mavrakos, "Numerical and experimental studies of a multi-purpose floating TLP structure for combined wind and wave energy exploitation," Mediterranean Marine Science, Vol. 20(4), pp. 745-763, 2019, doi.org/10.12681/mms.19366.